



# Dynamics of premixed CH<sub>4</sub>/air flames in a micro combustor with a plate flame holder and preheating channels



Jianlong Wan, Haibo Zhao\*

State Key Laboratory of Coal Combustion, School of Energy and Power Engineering, Huazhong University of Science and Technology, Wuhan, 430074, China

## ARTICLE INFO

### Article history:

Received 13 January 2017

Received in revised form

27 July 2017

Accepted 1 August 2017

Available online 1 August 2017

### Keywords:

Micro combustion

Plate flame holder

Preheating channel

Flame dynamics

Competitive effect

Thermal expansion

## ABSTRACT

It is challenging to achieve a wide flammable range in micro combustors due to the increased heat loss. In the present work, the flammable range based on equivalence ratio for a novel micro combustor is investigated, and some interesting dynamic flame behaviors are observed, which include the flame blow-off, pulsating flame and the flame with repetitive flashback and pulsating (FRFP). Our analysis indicates that the above flame behaviors mainly depend on the competition of the burning velocity and flow speed. For the lean fuel, a higher equivalence ratio leads to a faster burning velocity and a higher preheating temperature. A higher preheating temperature further elevates the burning velocity as well as the flow speed of incoming gas mixture. The faster burning velocity makes the flame shift upstream, but the bigger flow speed pushes the flame downstream. In such a way, the increase of equivalence ratio gives rise to the increase of burning velocity and flow speed, and the burning velocity increases faster than the flow speed. In addition, the flame dynamics distributions are almost symmetrical with respect to the stoichiometric ratio, *i.e.*, the flame behaviors under lean and rich fuel are the same basically.

© 2017 Elsevier Ltd. All rights reserved.

## 1. Introduction

As the hydrocarbon fuels possess much higher energy densities than the conventional electrochemical batteries, the power generation apparatus utilizing micro-scale combustion energy are considered as a promising alternative [1–3]. However, a sharp increase of heat-loss ratio due to the large surface-area-to-volume ratio for the micro-combustor obviously impacts the flame stability. Moreover, the short residence time of gaseous mixture easily leads to an incomplete combustion. These problems result in various dynamic flame behaviors in micro- and meso-scale combustors [4–8]. Therefore, it is crucial to develop the micro combustor with a wide operational range of the stable flame for the power-generation devices.

Many methods have been employed to improve flame stability in micro- and meso-scale combustors. Heat management is a frequently adopted strategy to improve flame stability in miniature combustors [9–11]. Epstein [12] and Spadaccini et al. [13,14] developed a micro-gas turbine engine with heat recirculation,

and their results indicate that this structure is beneficial for achieving stable combustion within a large range of inlet velocity. Kim et al. [15] and Kuo et al. [16] used the “Swiss-roll” configuration to stabilize lean flames in small combustors, and their results indicated that the flammability range of fuel mixture can be significantly extended. Gauthier et al. [17] found that the burning-rate in a small heat-recirculating tube can be enhanced, and this enhancement effect is not only caused by the preheating effect of solid wall, but also by the increase of flame front area. Jiang et al. [18] developed a low heat loss stainless steel combustor with porous media wall, and their experimental results showed that this structure is valid to utilize heat recirculation to stabilize the micro-flame. Wang et al. [19] pointed out that inert porous media which generates heat recirculation can significantly expand the operating limits of equivalence ratio of premixed methane/air. Baigomhammadi et al. [20] demonstrated that inserted wire can significantly improve the flame stability within the micro combustor. Veeraragavan [21] pointed out that the wall made of orthotropic thermal conductivity material creates “hot pockets” in the wall which can stabilize the flame propagation in a parallel plate burner.

Moreover, the flow recirculation zone generated in the combustion chamber is another effective approach to improve the flame stabilization. Yang et al. [22] found that the operational limits of inlet velocity in micro combustors with one backward facing step

\* Corresponding author. State Key Laboratory of Coal Combustion, Huazhong University of Science and Technology, 1037 Luoyu Road, Wuhan, 430074, China.

E-mail addresses: [klinsmannzhb@163.com](mailto:klinsmannzhb@163.com), [hzhao@hust.edu.cn](mailto:hzhao@hust.edu.cn) (H. Zhao).

## Nomenclature

$C_p$	specific heat capacity of fluid, J/(kg K)	$x$	horizontal distance of the combustor, m
$C_{p,i}$	specific heat capacity of species $i$ , J/(kg K)	$y$	vertical distance of the combustor, m
$C_s$	specific heat capacity of the solid material, J/(kg K)	$Y_{\text{HCO}}$	mass fraction of HCO radical
$D_{m,i}$	diffusion coefficient of species $i$ in the mixture, $\text{m}^2/\text{s}$	$Y_i$	mass fraction of species $i$
$f_i$	number of modes of energy storage (degree of freedom)	$\Delta x$	horizontal distance between two contiguous grids, m
$H_s$	natural convection heat transfer coefficient, $\text{W}/(\text{m}^2 \text{K})$	$\Delta y$	vertical distance between two contiguous grids, m
$M_W$	molecular weight of the gas	<b>Greeks</b>	
$M_{W,i}$	molecular weight of species $i$	$\varepsilon_s$	emissivity of the solid surface
$R_i$	generation or consumption rate of species $i$ , $\text{kg}/\text{m}^3 \text{ s}$	$\lambda_f$	thermal conductivity of fluid, $\text{W}/(\text{m K})$
$T_f$	fluid temperature, K	$\lambda_s$	thermal conductivity of the solid material, $\text{W}/(\text{m K})$
$T_s$	solid temperature, K	$\mu_i$	viscosity of species $i$ , $\text{kg}/(\text{m s})$
$T_{w,o}$	outer wall temperature, K	$\rho$	density of the fluid, $\text{kg}/\text{m}^3$
$T_\infty$	ambient temperature, K	$\rho_s$	density of the solid, $\text{kg}/\text{m}^3$
$v_x$	horizontal component of flow speed, $\text{m}/\text{s}$	$\delta$	wall thickness, m
$v_y$	vertical component of flow speed, $\text{m}/\text{s}$	$\sigma_s$	stephan-Boltzman constant, $\text{W}/(\text{m}^2 \text{K}^4)$
		$\phi$	equivalence ratio of mixture

are enlarged. Khandelwal et al. [23] experimentally demonstrated that the flame stability limits in the micro-combustor with three rearward steps are extended evidently. Wan et al. [24] developed micro- or meso-scale combustors with bluff-body which possess excellent flame stabilization performance. Moreover, Wan et al. [25,26] found that flame stability in the micro- or meso-scale combustor with cavities was also greatly improved. The premixed  $\text{CH}_4/\text{air}$  flames in the meso-scale cavity-combustor can keep stable and symmetric over a wide range of inlet velocity. However, under some severe operating conditions (such as low fuel concentration and high inlet velocity), some dynamic flame behaviors were observed by many researchers [27,28]. Pizza et al. [29] found five dynamic flame types which include periodic ignition and extinction, symmetric V-shaped, asymmetric, oscillating and pulsating flames in small plane channels using direct numerical simulation, and these flame dynamic behaviors were also experimentally and numerically observed by Brambilla et al. [30]. Baigmohammadi et al. [31] experimentally investigated the effects of several parameters (flow rate, equivalence ratio, oxygen concentration and the reactor diameter and length) on the flame dynamics of propane-air/oxygen in a non-adiabatic meso-scale combustor, and they found these factors can obviously affect the flame stability and propagation mode. Lee et al. [32] simulated the flame dynamics of lean  $\text{H}_2/\text{air}$  near the blow-off limit in a micro combustor with bluff body and clearly elucidated the flame blow-off mechanism in the combustor, and they pointed out that the narrow flow confinement may have a significant effect on the flame behavior [33]. These researches on dynamic flame behaviors are beneficial for understanding combustion phenomenon, and provide hints to improve flame stability further.

From the above review, it can be seen that the effects of the flow recirculation and heat recirculation on stabilizing the flame are significant. In order to further improve the flame stabilization, we developed a micro combustor with a plate flame holder and preheating channels in our recent publications [34,35]. This special configuration can take full advantages of both the flow recirculation and heat recirculation effects. We investigated the effects of the solid materials [34] and the length of the flame holder [35] on the flame blow-off limits systematically, and the results showed that lean  $\text{CH}_4/\text{air}$  premixed flames can be stabilized in this combustor within a large range of inlet velocity. This combustor can be used as heat resource for the micro- or meso-scale TPV (Thermophotovoltaic) and propulsion systems. However, the flammability limits

of equivalence ratio and flame dynamic behaviors of methane/air premixed gaseous mixture in this kind of combustor are not studied yet, especially when keeping in mind that there usually exist different flame behaviors at different equivalence ratios. Understanding the combustion characteristics and underlying mechanisms in this combustor will be beneficial for the application of this combustor. In the present work, the flammable range based on equivalence ratio is investigated. Meanwhile, some kinds of flame dynamic behaviors are also observed in details. The underlying mechanisms are analyzed in terms of the heat recirculation, chemical reactions, flow field, stretching effect and heat loss.

## 2. Numerical methods

### 2.1. Geometric model

Fig. 1 schematically shows a two-dimensional, symmetric combustor with a plate flame holder and preheating channels. For clarity, two yellow solid lines are used to divide the whole channel of the combustor into two segments, i.e., the preheating channel and the combustion chamber. Additionally, the red dashed lines divide the combustor solid wall into six segments. They are the plate flame holder, one external wall of the preheating channels, two internal walls of the preheating channels and two combustion chamber walls. The geometry dimension is also shown in Fig. 1. The wall thickness ( $\delta$ ) is 0.5 mm, and the length of the plate flame holder is 6.0 mm. In addition, further refinement of the meshes near the plate flame holder is conducted, and a non-uniform grid system with 23,925 cells is employed in final computation [35].

### 2.2. Mathematical model

Here, the inlet velocity (flow speed at the inlet of combustor) is fixed at 2 m/s, and the corresponding Reynolds number of the incoming cold mixture is around 80. Then, the equivalence ratio ( $\phi$ ) of incoming mixture is changed with a step of 0.025 to obtain the operating range of equivalence ratio which corresponds to different flame dynamic behaviors. Therefore, laminar flow and unsteady state models are used in the computation. Governing equations for the gaseous mixture are shown in Table 1. The incompressible flow is considered here because, the flow speed and pressure variation in the combustor are small comparing with the sound speed of the gaseous mixture, therefore the compressibility effects can be

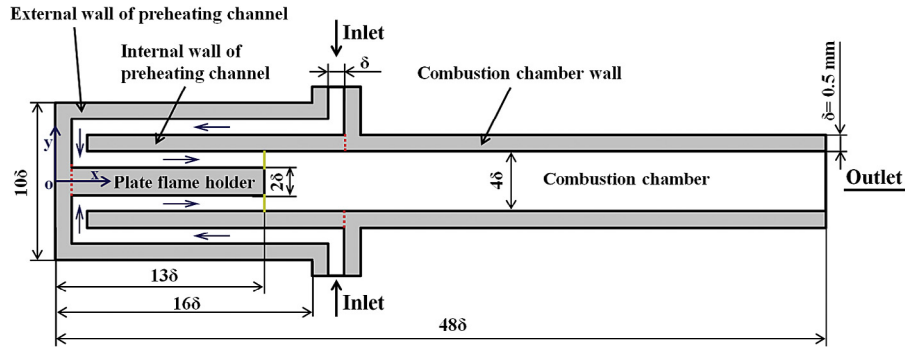


Fig. 1. Schematic of the micro combustor with a plate flame holder and preheating channels.

Table 1

Governing equations and constitutive correlations in the model.

#### Continuity equation

$$\frac{\partial \rho}{\partial t} + \frac{\partial}{\partial x}(\rho v_x) + \frac{\partial}{\partial y}(\rho v_y) = 0 \quad (1)$$

#### Momentum equations

$$\frac{\partial(\rho v_x)}{\partial t} = - \left[ \frac{\partial(\rho v_x v_x)}{\partial x} + \frac{\partial(\rho v_x v_y)}{\partial y} \right] - \frac{\partial p}{\partial x} + \frac{\partial \tau_{xx}}{\partial x} + \frac{\partial \tau_{xy}}{\partial y} \quad (2)$$

$$\frac{\partial(\rho v_y)}{\partial t} = - \left[ \frac{\partial(\rho v_y v_x)}{\partial x} + \frac{\partial(\rho v_y v_y)}{\partial y} \right] - \frac{\partial p}{\partial y} + \frac{\partial \tau_{yx}}{\partial x} + \frac{\partial \tau_{yy}}{\partial y} \quad (3)$$

#### Energy equation

$$\begin{aligned} \frac{\partial(\rho C_p T_f)}{\partial t} + \frac{\partial(\rho v_x C_p T_f)}{\partial x} + \frac{\partial(\rho v_y C_p T_f)}{\partial y} &= \frac{\partial(\lambda_f \partial T_f)}{\partial x^2} + \frac{\partial(\lambda_f \partial T_f)}{\partial y^2} \\ + \sum_i \left[ \frac{\partial}{\partial x} \left( C_{p,i} T_f \rho D_{m,i} \frac{\partial Y_i}{\partial x} \right) + \frac{\partial}{\partial y} \left( C_{p,i} T_f \rho D_{m,i} \frac{\partial Y_i}{\partial y} \right) \right] &+ \sum_i C_{p,i} T_f R_i \end{aligned} \quad (4)$$

#### Species equation

$$\frac{\partial(\rho Y_i)}{\partial t} + \frac{\partial(\rho Y_i v_x)}{\partial x} + \frac{\partial(\rho Y_i v_y)}{\partial y} = \frac{\partial}{\partial x} \left( \rho D_{m,i} \frac{\partial Y_i}{\partial x} \right) + \frac{\partial}{\partial y} \left( \rho D_{m,i} \frac{\partial Y_i}{\partial y} \right) + R_i \quad (5)$$

#### Properties

Mass-averaged viscosity, specific heat and thermal conductivity

$$\text{Viscosity: } \mu = \sum_i Y_i \mu_i, \text{ with } \mu_i = 2.67 \times 10^{-6} \frac{\sqrt{M_w T}}{\sigma^2 \Omega_\mu} \quad (6)$$

$$\text{Specific heat: } C_{p,f} = \sum_i Y_i C_{p,i}, \text{ with } C_{p,i} = \frac{1}{2} \frac{R}{M_{w,i}} (f_i + 2) \quad (7)$$

$$\text{Thermal conductivity: } \lambda_f = \sum_i Y_i \lambda_{f,i}, \text{ with } \lambda_{f,i} = \frac{15}{4} \frac{R}{M_{w,i}} \mu_i \left[ \frac{4}{15} \frac{C_{p,i} M_{w,i}}{R} + \frac{1}{3} \right] \quad (8)$$

Energy equation for the solid walls

$$\frac{\partial}{\partial x} \left( \lambda_s \frac{\partial T_s}{\partial x} \right) + \frac{\partial}{\partial y} \left( \lambda_s \frac{\partial T_s}{\partial y} \right) = \frac{\partial(\rho_s c_s T_s)}{\partial t} \quad (9)$$

negligible and the variation of the gas density with pressure can also be ignored. To be noted, the density of gaseous mixture in the combustion process will be changed as temperature, however this density change is induced by the thermal expansion effect, not pressure variation. The heat transfer in the combustor walls is also considered in the computation, since the heat conduction in the solid walls can observably affect the combustion process and flame propagation characteristics [21].

### 2.3. Computation scheme

The fuel and oxidizer are methane and air, respectively. As we known, the Lewis number of methane/air is ~1. It is considered here that the effect of Lewis number is not so remarkable in this case. The stainless steel, which is often used to manufacture the micro combustor [15,36,37], is used as solid material, whose density, specific heat capacity and thermal conductivity are 8000 kg/m<sup>3</sup>,

500 J/(kg·K) and 24 W/(m·K), respectively [38]. The detailed C1 chemistry mechanism [39], which includes 18 species and 58 elementary reactions, is adopted to simulate CH<sub>4</sub>/air premixed combustion. The 18 species include some unstable prominent radicals, such as H, CH, CH<sub>2</sub>, CH<sub>3</sub> and CH<sub>2</sub>O, and some stable species (i.e., H<sub>2</sub>O and CO<sub>2</sub>). The 58 elementary reactions include four main initiation reactions of methane oxidation (i.e., CH<sub>4</sub>+O<sub>2</sub>=CH<sub>3</sub>+HO<sub>2</sub>, CH<sub>4</sub>+H=CH<sub>3</sub>+H<sub>2</sub>, CH<sub>4</sub>+O=CH<sub>3</sub>+OH and CH<sub>4</sub>+OH=CH<sub>3</sub>+H<sub>2</sub>O) and eight chemical reactions which contain five kinds of third body (i.e., H<sub>2</sub>O, CO<sub>2</sub>, H<sub>2</sub>, CO and N<sub>2</sub>), and other chemical reactions. The thermodynamic and transport properties of the gaseous species are taken from the CHEMKIN databases [40,41]. The method of “two-sided walls” is used to calculate the internal heat transfer between the gaseous mixture and solid [42]. For the wall zone has a fluid and a solid region on each side (called the “two-sided wall”), a “shadow” zone is created so that each side of the wall is a distinct wall zone, and the method of “Coupled” is adopted to calculate heat transfer directly from the profiles in the adjacent cells. The heat loss rate from the outer wall surfaces of the combustor is calculated by  $q = h_s(T_{w,o} - T_\infty) + \epsilon_s \sigma_s (T_{w,o}^4 - T_\infty^4)$ , where  $T_{w,o}$  is the outer wall temperature,  $T_\infty$  is the ambient temperature,  $h_s$  is the natural convection heat transfer coefficient,  $\epsilon_s$  is the wall surface emissivity, and  $\sigma_s$  is the Stephan-Boltzmann constant. Table 2 displays the boundary conditions for numerical simulation.

The frequently used computational fluid dynamics software, FLUENT 6.3 [42], is applied to solve the momentum, mass, energy and species conservation equations. Only half of configuration is adopted in the simulation to reduce the computation load. In addition, grid independency test is conducted using three sets of grid system ( $\Delta x = \Delta y = 50 \mu\text{m}$ ,  $40 \mu\text{m}$  and  $25 \mu\text{m}$ , respectively). When comparing the profiles of two key radicals (HCO and OH) near the flame front, it is found that the cell size of  $50 \mu\text{m}$  has been sufficiently fine to capture the flame structure [35]. Considering both computation accuracy and load, a time step of  $1.0 \times 10^{-5}$  s is selected for the unsteady state simulation. Our previous simulations [24,25,35] have demonstrated that the time step of  $1.0 \times 10^{-5}$  s is suitable to capture the flame behaviors correctly in the micro- or meso-scale combustor. Convergence of the numerical simulation is based on the residuals of all governing equations to be less than  $1.0 \times 10^{-6}$ .

### 3. Results and discussions

#### 3.1. Flame behaviors in the combustor at different equivalence ratios

Fig. 2 shows the premixed flame dynamics of CH<sub>4</sub>/air in the micro combustor with a plate flame holder and preheating channel.

From this figure, it can be seen that the flame blows off at  $\phi = 0.50$ , i.e.,  $\phi = 0.50$  is the lean flammability limit. The flame will break away from the right wall ( $x = 6.5 \text{ mm}$ ) of plate flame holder firstly, and then shift to the downstream channel. In the end, the flame blows out of the combustion chamber. When the equivalence ratio increases from 0.5 to 0.525, the flame will become stable in the combustion chamber. The flame keeps stable until  $\phi = 0.7$ . In addition, the length of the flame front is decreasing with the increase of equivalence ratio until 0.7. Then, at  $\phi = 0.725$ , the flame becomes a pulsating behavior with a small amplitude in the combustion chamber. With a further increase of equivalence ratio ( $\phi = 0.75$ ), the flame with repetitive flashback and pulsating (FRFP) will occur. The FRFP is the flame behavior that the flame flashes back to the preheating channel firstly, and then blows out of the preheating channel and becomes a pulsating mode in the combustion chamber. Later, the flame flashes back to the preheating channel again. This phenomenon repetitively occurs at the equivalence ratio between 0.75 and 1.30. If the equivalence ratio still increases to 1.325 and 1.35, the flame becomes pulsating in the combustion chamber, which is similar to the flame behavior at  $\phi = 0.725$ . Further, at  $\phi = 1.375$ , the flame reverts to a stable behavior in the combustion chamber. However, for a larger equivalence ratio ( $\phi = 1.40$ ), the flame will blow off, and the process and mechanism of flame blow-off under rich fuel are similar with these at  $\phi = 0.50$ .

Obviously, the flame dynamics distributions are almost

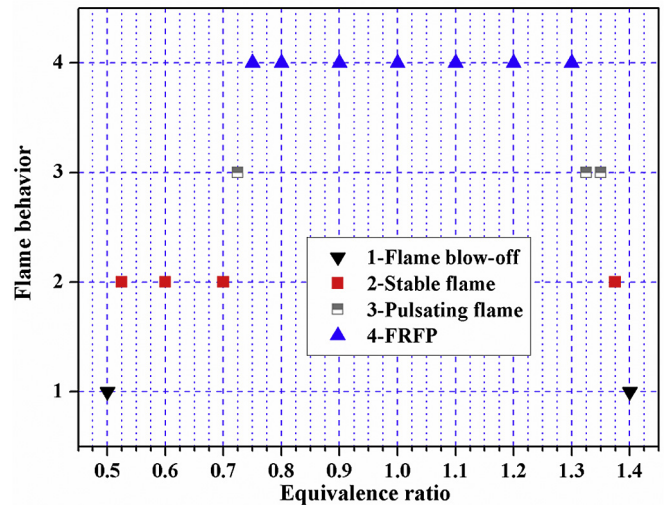


Fig. 2. Flame behaviors in the combustor with a plate flame holder and preheating channels for different equivalence ratios under the small inlet velocity.

Table 2  
Boundary conditions for numerical simulation.

Position	Settings
Inner wall surfaces	Chemically inert with no-slip
Inlet of combustor	Uniform concentration and velocity distributions of 2.0 m/s with 300 K
Outlet of combustor	Neumann boundary
Heat flux in the solid wall and fluid	Fourier's law
Heat loss from the outer wall surfaces	Including natural convection and radiation
Natural convection heat transfer coefficient	$20 \text{ W m}^{-2} \text{ K}^{-1}$
Wall surface emissivity	0.2
Ambient temperature	300 K
Stephan-Boltzmann constant	$5.67 \times 10^{-8} \text{ W m}^{-2} \text{ K}^{-4}$
Internal heat transfer between the fluid and solid	The method of “Coupled”
Coupling the pressure and velocity	The “SIMPLE” algorithm
Initial ignition temperature	2000 K
Time step	$1.0 \times 10^{-5} \text{ s}$

symmetrical with respect to the stoichiometric ratio, *i.e.*, the flame behaviors under lean and rich fuel are the same basically. However, the equivalence ratio range under normal temperature and pressure are  $\sim 0.6\text{--}1.3$  [44], which are not completely symmetrical with respect to  $\phi = 1.0$ . Moreover, many researchers have pointed out that the burning velocity of premixed methane/air reaches the biggest value at  $\sim \phi = 1.05$  [44], and the decreasing amplitude of burning velocity with the increase of equivalence ratio under rich fuel is larger than that of burning velocity with the decrease of equivalence ratio under lean fuel. The flame behavior is mainly determined by the competitive effect of the burning velocity and flow speed, which will be detailedly discussed in the following sections. Therefore, the small difference in the change of burning velocity with the equivalence ratio makes the flame behavior distribution under lean fuel a little different from that under rich fuel. For example, the equivalence ratio range of stable flame under lean fuel is wider than that under rich fuel, which is possibly caused by a smaller decreasing amplitude of the burning velocity under lean fuel. For the purpose of concision, we just display some representative cases which include the flame blow-off, stable flame, pulsating flame and FRFP for the lean fuels in the following sections.

### 3.2. Stable flame

In our previous work [34], we used the normalized 15% maximum mass fraction of HCO ( $Y_{\text{HCO}}$ ) isoline to visualize the flame front. Here, we use the same definition for the flame front. Moreover, the flame front near the right wall of flame holder ( $x = 6.5$  mm,  $-0.5$  mm  $\leq y \leq 0.5$  mm) and near the combustion chamber wall ( $y = 1.0$  mm) are defined as flame root and flame tip, respectively. The horizontal distance between the flame root and flame tip is the length of the flame front. As known, a higher equivalence ratio leads to a faster burning velocity and a higher preheating temperature of incoming unburned mixture for the lean fuel. In addition, a higher preheating temperature will lead to a faster burning velocity [45], as well as a bigger flow speed of incoming unburned mixture due to a more significant thermal expansion effect. It is known that the faster burning velocity makes the flame shift upstream, but the bigger flow speed will enlarge the stretching effect on the flame front and push the flame downstream. In summary, as the equivalence ratio increases, the burning velocity and flow speed of incoming unburned mixture increase with an increasing preheating effect on mixture, and the burning velocity increases faster than the flow speed. The flame behavior is mainly determined by the competitive effect of the burning velocity and flow speed. Fig. 2 shows that the flame at the equivalence ratio between 0.525 and 0.7 is stable. This is mainly because that the burning velocity can reach a balance with the flow speed at a certain location near the inlet of combustion chamber in this stage. With the increase of equivalence ratio, although the burning velocity increases faster than the flow speed, the shape of flame front is changed at the same time, and the length of the flame front decreases (see Fig. 3), which increases normal component of the flow speed of incoming unburned mixture to against the increasing burning velocity. That is why the flame can remain stable within a range of equivalence ratio rather than a certain equivalence ratio. For instance, Fig. 3 shows the temperature contours with overlaid 15% maximum  $Y_{\text{HCO}}$  isoline (blue solid line) at  $\phi = 0.700$ , 0.600 and 0.525. It can be seen that the combustor temperature level is increasing with an increasing equivalence ratio. This is mainly because that the fuel mixture with a larger equivalence ratio can release more heat energy, which will increase the temperature level of combustor. As a result, the incoming gas temperature at the inlet of combustion chamber ( $x = 6.5$  mm,  $0.5$  mm  $\leq y \leq 1.0$  mm) is higher for a larger equivalence ratio, as depicted in Fig. 4. Fig. 4

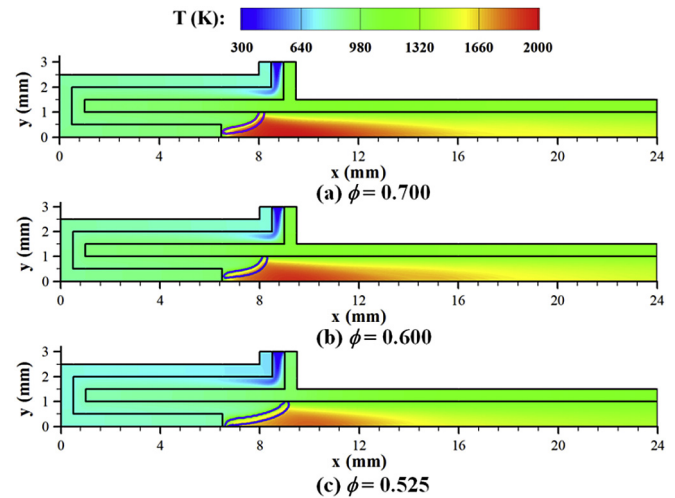


Fig. 3. Temperature contours with overlaid 15% maximum  $Y_{\text{HCO}}$  isoline (blue solid line) at  $\phi = 0.700$ , 0.600 and 0.525. (For interpretation of the references to colour in this figure legend, the reader is referred to the web version of this article.)

shows that the average gas temperature of incoming mixture at  $\phi = 0.700$  is around 120 K higher than that at  $\phi = 0.525$ . This will certainly influence the flame shape and length.

Fig. 5 presents the temperature contours with overlaid velocity isolines of  $x$  direction (black solid lines) and 15% maximum  $Y_{\text{HCO}}$  isoline (blue solid line) near the flame front ( $6.0$  mm  $\leq x \leq 10.0$  mm) at  $\phi = 0.700$ , 0.600 and 0.525. It can be seen that the flame length increases from 1.68 mm at  $\phi = 0.700$ –2.57 mm at  $\phi = 0.525$ . This is because that a better preheating effect on the incoming unburned mixture not only increases the burning velocity, but also makes the fuel ignite early and induces the initiation reactions of methane oxidation. Therefore, the flame tip shifts downstream, which is also represented by the vertical black dashed line in Fig. 5. Moreover, the flame root shifts to the center axis of combustor with a decrease of equivalence ratio. At  $\phi = 0.525$ , the upper flame front ( $0.0$  mm  $\leq y \leq 1.0$  mm) merges with the lower flame front ( $-1.0$  mm  $\leq y \leq 0.0$  mm) behind the flame holder (see Fig. 5b). The movement tendency of flame root can also be seen in Fig. 6a. Moreover, Fig. 6a shows that the maximum of  $Y_{\text{HCO}}$  increases with

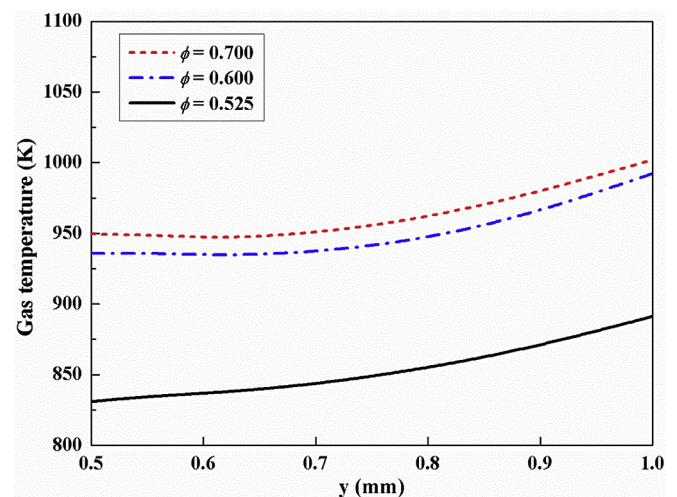
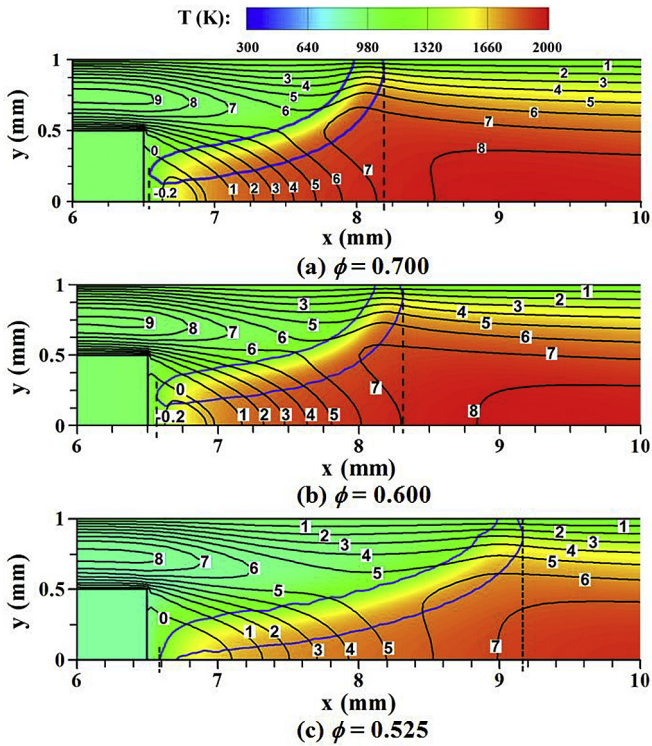
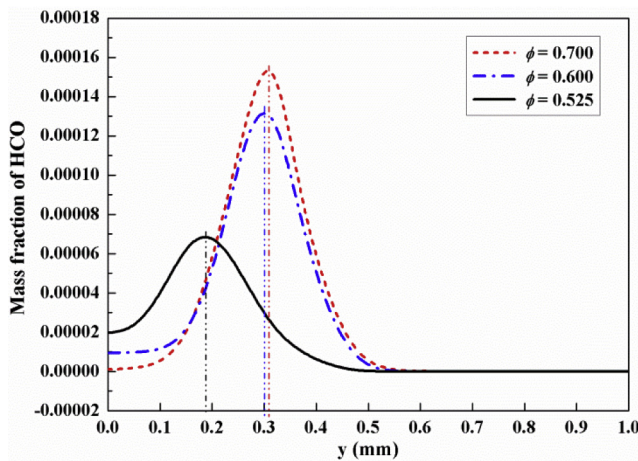


Fig. 4. Temperature profiles at the inlet of combustion chamber ( $x = 6.5$  mm,  $0.5$  mm  $\leq y \leq 1.0$  mm) at  $\phi = 0.700$ , 0.600 and 0.525.

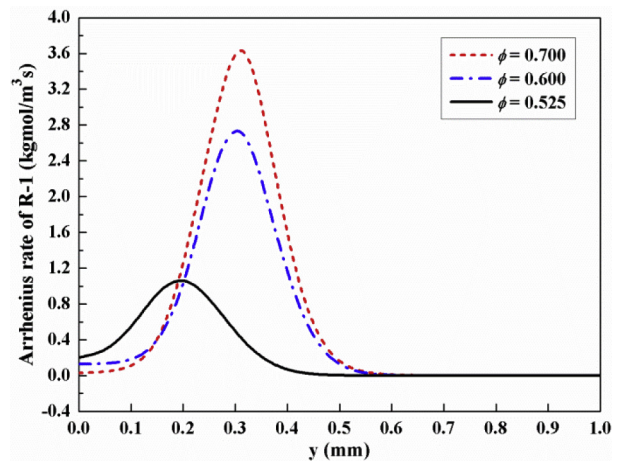


**Fig. 5.** Temperature contours with overlaid velocity isolines of  $x$  direction (black solid lines) and 15% maximum  $Y_{HCO}$  isoline (blue solid line) near the flame front ( $6.0 \text{ mm} \leq x \leq 10.0 \text{ mm}$ ) at  $\phi = 0.700, 0.600$  and  $0.525$ . (For interpretation of the references to colour in this figure legend, the reader is referred to the web version of this article.)

an increasing equivalence ratio. This is mainly because that the combustion reaction is more intense for a higher equivalence ratio (as shown in Fig. 6b). Nikolaou and Swaminathan [46] pointed out that for  $CH_4$ /air premixed mixture, the rate of chemical reaction:  $H + CH_2O = HCO + H_2$  (to be referred as R-1 thereafter) serves to be an unambiguous and good marker of heat release rate. Here, we show the reaction rate of R-1 near the flame root ( $x = 7.0 \text{ mm}$ ,  $0 \text{ mm} \leq y \leq 1 \text{ mm}$ ) in Fig. 6b. It is evident that the maximum



(a)



(b)

**Fig. 6.** Mass fraction of HCO (a) and reaction rate of R-1 ( $H + CH_2O = HCO + H_2$ ) (b) near the flame root ( $x = 7.0 \text{ mm}$ ,  $0.0 \text{ mm} \leq y \leq 1.0 \text{ mm}$ ) at  $\phi = 0.700, 0.600$  and  $0.525$ .

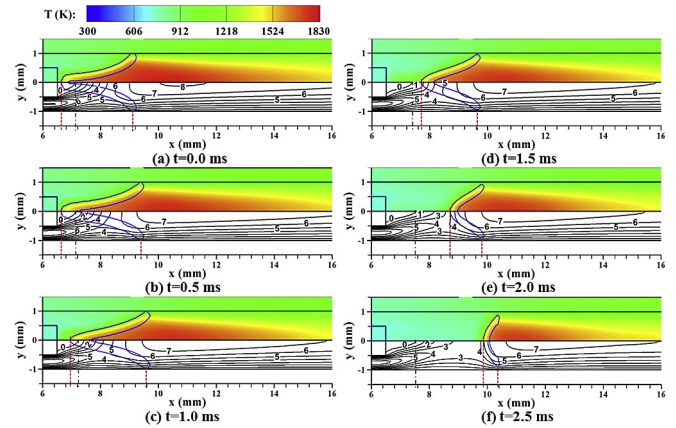


**Fig. 7.** Temperature contours and velocity field (black lines) with overlaid 15% maximum  $Y_{HCO}$  isoline (blue solid line) at  $\phi = 0.50$ . (For interpretation of the references to colour in this figure legend, the reader is referred to the web version of this article.)

reaction rate of R-1 is consistent with the mass fraction of HCO and preheating temperature levels (see Figs. 6a and 3). The maximum of reaction R-1 at  $\phi = 0.700$  is nearly 3.6 times larger than that at  $\phi = 0.525$ . Therefore, a higher equivalence ratio favors the exothermal reaction of  $CH_4$ /air mixture.

### 3.3. Flame blow-off at $\phi = 0.50$

Fig. 7 shows the temperature contours and velocity field (black lines) with overlaid 15% maximum  $Y_{HCO}$  isoline (blue solid line) at  $\phi = 0.50$ . From the above results, it can be known that the length of flame front is larger for a smaller equivalence ratio. When the equivalence ratio decreases to 0.5, the heat release rate of fuel becomes smaller, which leads to a weaker preheating effect on the incoming unburned mixture. Moreover, the heat loss of the outer wall surface further reduces the gas temperature at the inlet of combustion chamber ( $x = 6.5 \text{ mm}$ ) and the right wall ( $x = 6.5 \text{ mm}$ ,  $-0.5 \text{ mm} \leq y \leq 0.5 \text{ mm}$ ) temperature of flame holder with time (see Fig. 8). Fig. 8 shows the gas and wall temperature profiles at the inlet section of combustion chamber ( $x = 6.5 \text{ mm}$ ), which presents that the gas temperature and right wall

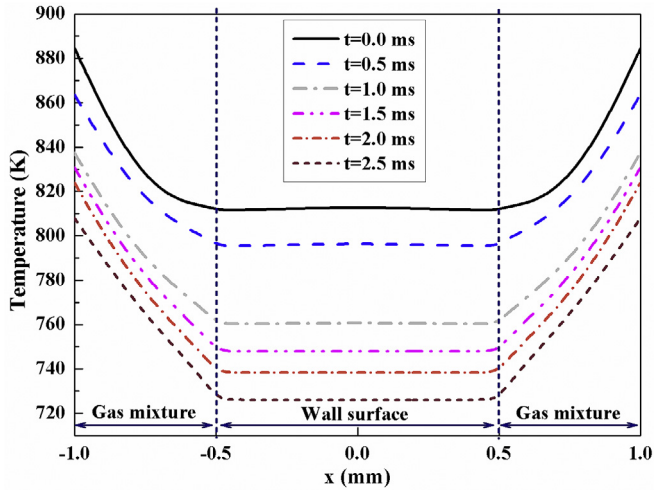


Fig. 8. Gas and wall temperature profiles at the inlet section of combustion chamber ( $x = 6.5$  mm,  $-1$  mm  $\leq y \leq 1.0$  mm) at  $\phi = 0.50$ .

temperature decrease with time. Additionally, it is worth noting that the temperature decreases faster at the earlier process ( $0.0$  ms  $\leq t \leq 1.0$  ms) of flame blow-off. This is because the heating effect of flame on the right wall of flame holder sharply decreases with the increase of the distance between the flame root and right wall. As a result, the burning velocity is small and the right wall temperature of flame holder is low. Therefore, even though the flame root is in the recirculation zone behind the flame holder (as the blue dash-dot lines shown), the flame root is pushed away from the right wall ( $x = 6.5$  mm,  $-0.5$  mm  $\leq y \leq 0.5$  mm) of flame holder by the incoming unburned gaseous mixture, and the flame tip shifts downstream along with the combustion chamber wall (see the red dashed lines in Fig. 7a, b and c). In turn, the incoming gas temperature and right wall temperature of flame holder decrease to a lower level (see Fig. 8), which leads to a further movement of the flame to the exit of the combustor ( $x = 24.0$  mm). After  $t = 1.0$  ms, the flame tip shifts downstream very slowly, but the flame root shifts downstream significantly (see Fig. 7d). This is mainly because that the inner wall temperature of combustion chamber attached by the flame tip is relatively high. In other words, the length of the flame front decreases from 2.61 mm at  $t = 1.0$  ms to 1.92 mm at  $t = 1.5$  ms, and the flame root totally breaks away from the recirculation zone behind the flame holder. Then, the flame root and flame tip shift downstream obviously, and the travelling speed of flame root is faster than that of the flame tip (see Fig. 7e and f). The length of flame front decreases from 1.92 mm at  $t = 1.5$  ms to 0.53 mm at  $t = 2.5$  ms. Moreover, the curvature rate of flame tip decreases as time. Finally, the flame will be totally blown out of the combustion chamber. Additionally, the flame blow-off process and mechanism under rich fuel are similar with that under the present lean case. The total flame also breaks away from the right wall of flame holder at first and then shifts downstream, and the flame is blown out of the combustor in the end. This is mainly because the heat release rate of fuel mixture is also smaller at the rich flammability limit.

### 3.4. Pulsating flame

The pulsating flame will occur in the combustion chamber when the equivalence ratio increases to 0.725, as shown in Fig. 9. The flame is slightly pulsating with time. It is believed that a faster burning velocity plays main role in the movement of flame front. The flame front firstly shifts to the inlet of combustion chamber

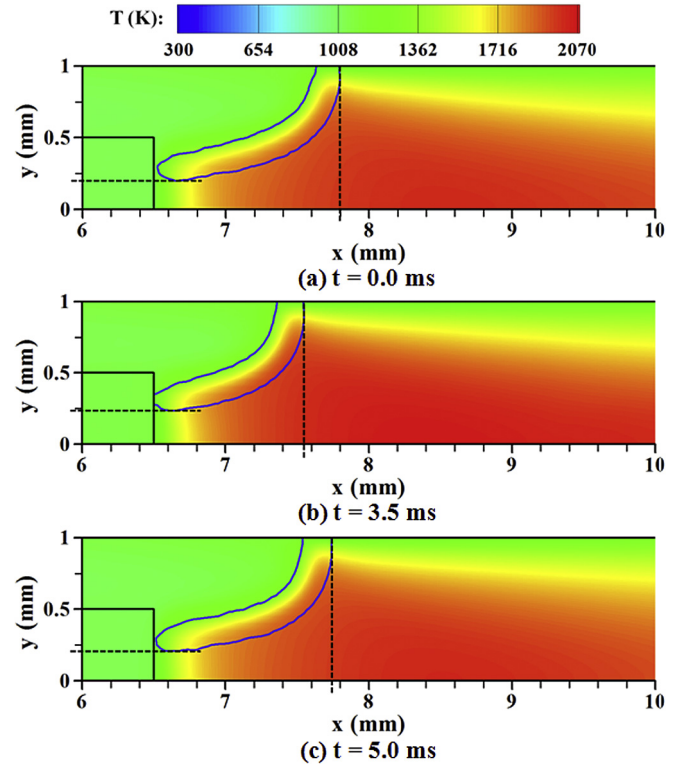


Fig. 9. Temperature contours with overlaid 15% maximum  $Y_{HCO}$  isoline (blue solid line) at  $\phi = 0.725$ . (For interpretation of the references to colour in this figure legend, the reader is referred to the web version of this article.)

( $x = 6.5$  mm, see Fig. 9b). However, the burning velocity under the present preheating temperature and equivalence ratio is not fast enough to compete against the flow speed of incoming unburned mixture near the inlet of combustion chamber, which thereby makes the flame flash back to the preheating channel. Then, the flame will shift downstream again. The mechanism for this dynamic behavior can be illustrated in Fig. 10. Fig. 10 presents the dynamic feedback loop between flame location, heat recirculation effect, burning velocity and flow speed for the pulsating flame in the combustion chamber. At  $\phi = 0.725$ , the burning velocity is faster, and a larger heat release quantity enhances the heat recirculation effect through solid wall on the incoming unburned mixture, which further enlarges the burning velocity. As a result, the burning velocity ( $S_L$ ) at the location of 1 in Fig. 10 is bigger than the normal component ( $V_{1,n}$ ) of flow velocity near the flame front firstly. Hence, the flame front shifts to the location of 2. However, when the flame shifts to the location of 2,  $\theta$  is larger, which results

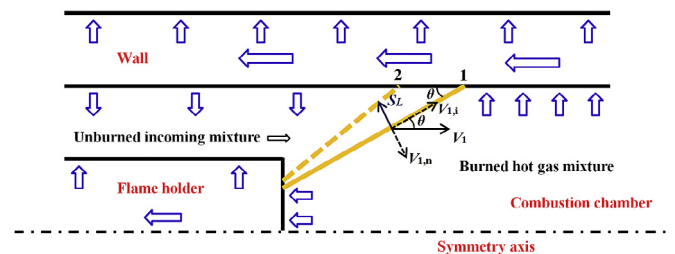


Fig. 10. Schematic of the interactions between the flame front, solid wall and gas mixture in the combustion chamber (the blue arrow indicates the direction of heat flux). (For interpretation of the references to colour in this figure legend, the reader is referred to the web version of this article.)

in the increment of normal component of flow velocity, so the flame front is pushed to the location of 1 in Fig. 10 again. This back and forth movements of flame front occur repetitively.

The movements of the flame root and flame tip can be observed in Fig. 11. Fig. 11 shows the mass fraction profiles of HCO near the flame root ( $x = 6.6$  mm,  $0.0$  mm  $\leq y \leq 1.0$  mm) and flame tip ( $y = 0.975$  mm,  $7.0$  mm  $\leq x \leq 8.0$  mm) at  $\phi = 0.725$ . Fig. 11 also presents that the maximum of  $Y_{HCO}$  is the biggest at  $t = 3.5$  ms, which means that the chemical reaction at this time is more intense. After  $t = 3.5$  ms, the flame front will be pushed away from the inlet of combustion chamber (see Figs. 9c and 11). The reasons are related to the curvature of flame front and strain rate distributions at the inlet of combustion chamber ( $x = 6.5$  mm,  $0.5$  mm  $\leq y \leq 1.0$  mm), as shown in Fig. 12. It is calculated from Fig. 12a that the mean flow velocities at the inlet of combustion chamber at  $t = 0.0$  ms,  $3.5$  ms and  $5.0$  ms are  $5.91$  m/s,  $6.01$  m/s and  $5.93$  m/s, respectively, i.e., the flow speed at  $t = 3.5$  ms is the biggest, which leads to the biggest strain rate (the mean strain rates at the inlet of combustion chamber at  $t = 0.0$  ms,  $3.5$  ms and  $5.0$  ms are  $62466$  1/s,  $62628$  1/s and  $62509$  1/s, respectively). Moreover, Fig. 11 shows that the curvature of the flame front at  $t = 3.5$  ms is also the largest. As the flame stretch depends on both the curvature and strain rate [45], it can be deduced that the stretching effect on the flame front at  $t = 3.5$  ms is the largest. At this moment, the faster flow speed plays a key role in the movement of the flame front, which makes the flame blow away from the inlet of combustion chamber (see Fig. 9c). Then, the flame shape will return back to that at  $t = 0$  ms in Fig. 9a (see the red arrow which is named as 3 in Fig. 11b). The pulsating frequency at  $\phi = 0.725$  is  $\sim 167$  Hz, which is smaller than these at  $\phi = 1.325$  and  $1.350$  ( $201$  Hz and  $183$  Hz, respectively).

3.5. Flame with repetitive flashback and pulsating (FRFP)

Figs. 13, 18 and 20 show the total FRFP behavior at  $\phi = 0.75$ . From the above results we know that a higher equivalence ratio leads to a higher preheating temperature of incoming unburned mixture before entering into the combustion chamber. Different from the case of  $\phi = 0.725$ , the faster burning velocity at  $\phi = 0.75$  makes the flame shift upstream and further enhances the heat recirculation effect on the incoming unburned mixture, which further promotes the movement of flame to upstream location. As a result, the flame flashes back to the preheating channel at  $\phi = 0.75$ , as shown in Fig. 13b. In turn, the temperatures of preheating channel internal wall (see Fig. 14) and incoming mixture (see Fig. 13c) increase further. The flame in the combustion chamber flashes back to the preheating channel (see the flame front of 1 (defined as 1-flame) in Fig. 13c). Meanwhile, Fig. 14 shows that the internal wall surface

temperature of preheating channel increases significantly with time. The wall temperature even reaches  $1320$  K at  $t = 1.0$  ms, which is higher than the corresponding ignition temperature of incoming unburned mixture. As a result, the incoming mixture will be ignited at the location of 3-flame in Fig. 13c. This is because that the flow speed (not too large) and unburned preheating temperature (high enough) near this zone are more beneficial for the flame generation than other zones in preheating channel. Then, the 3-flame leads to a higher wall temperature, which subsequently results in the formation of 2-flame. Meanwhile, the fuel mixture between the 1-flame and 2-flame and that between the 2-flame and 3-flame are not completely consumed at once. In turn, the 2-flame and 3-flame further enhance the internal wall temperature of preheating channel (as shown in Fig. 14 at  $t = 2.0$  ms). Therefore, the high internal wall temperature of preheating channel makes the lower boundary of 3-flame shift to the external wall of preheating channel (see the red arrow in Fig. 13c). Later, the 3-flame in Fig. 13c will split into two parts, i.e., the new 3-flame and 4-flame in Fig. 13d, and the 3-flame shifts upstream and 4-flame shifts downstream (see the red arrow in Fig. 13d). The reasons which lead to the movements of 3-flame and 4-flame can be attained from Fig. 15a. Fig. 15a shows the mass fractions of HCO and  $CH_4$  with the flow speed profiles near the 3-flame. It can be seen that the methane between 3-flame and 4-flame is nearly completely consumed, so the thermal expansion effect makes the flow speed in this zone ( $\sim 1.75$  mm  $\leq x \leq 3.50$  mm) larger than that of its upstream and downstream zones. Moreover, the burned mixture with higher temperature in this zone (see Fig. 13d) elevates the burning velocities of 3-flame and 4-flame. However, the reasons which lead to the movements of 3-flame and 4-flame are not completely same. For the 3-flame, only the faster burning velocity makes it shift upstream. For the 4-flame, both the faster flow speed and burning velocity make it shift downstream. Meanwhile, the 2-flame also splits into the 5-flame and a new 2-flame (see Figs. 13e and 15b). Fig. 15b also illustrates why the 2-flame splits. Fig. 15b shows that the maximum of  $Y_{HCO}$  increases with time, which means that the reaction intensity of 2-flame is increasing, and the fuel is continually consumed (see the variation trend of the finest lines). When the fuel near the middle zone of 2-flame is nearly completely consumed ( $\sim 1.9$  mm  $\leq x \leq 2.1$  mm), the chemical reaction near the middle zone of 2-flame will be terminated, but the left and right edge zones of 2-flame have enough fuel to maintain combustion reaction. Therefore, the 2-flame at  $t = 2.02$  ms splits into a new 2-flame and 5-flame at  $t = 2.05$  ms. Then, like the 3-flame, the faster burning velocity makes the 5-flame shift upstream. For the new 2-flame, the faster flow speed and burning velocity make it shift downstream.

In addition, a new flame (5-flame in Fig. 13d) is generated at the

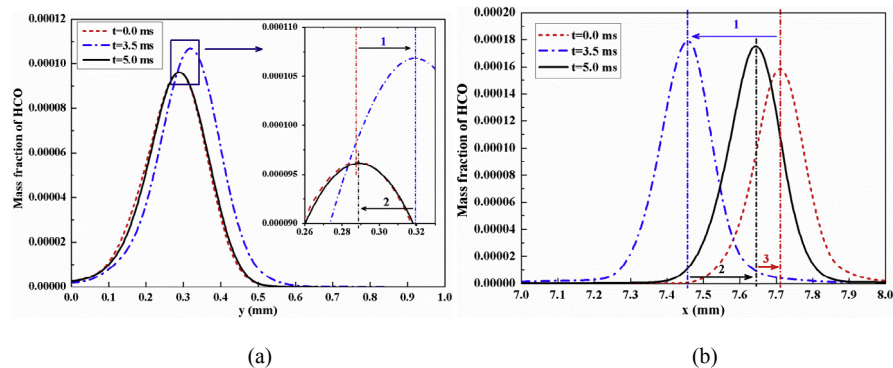


Fig. 11. Mass fraction profiles of HCO near the flame root ( $x = 6.6$  mm,  $0.0$  mm  $\leq y \leq 1.0$  mm) (a) and the flame tip ( $y = 0.975$  mm,  $7.0$  mm  $\leq x \leq 8.0$  mm) (b) at  $\phi = 0.725$ .

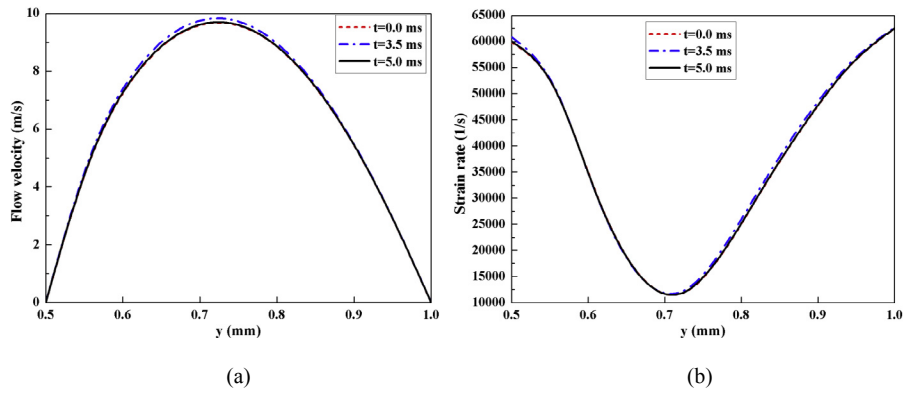


Fig. 12. Flow speed (a) and strain rate (b) at the inlet of combustion chamber ( $x = 6.5$  mm,  $0.5$  mm  $\leq y \leq 1.0$  mm) at  $\phi = 0.725$ .

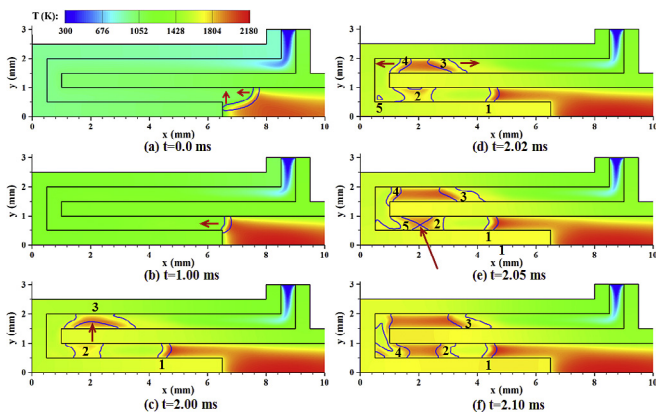


Fig. 13. Temperature contours with overlaid 15% maximum  $Y_{H_2CO}$  isoline (blue solid line) at  $\phi = 0.75$ , and the number in figure are used to indicate the flame front (the first part of FRFP). (For interpretation of the references to colour in this figure legend, the reader is referred to the web version of this article.)

turning point of preheating channel due to a high wall temperature of flame holder (see Fig. 16, which results from the heating effects of 1-flame and 2-flame on the preheating channel wall in Fig. 13c). From Fig. 16, it can be known that the upper wall temperature of

flame holder increases sharply from  $t = 1.00$  ms to  $t = 2.00$  ms, which will ignite the fuel mixture near the bottom of flame holder ( $x = 0.50$  mm). Moreover, the left boundary and right boundary of 2-flame shift upstream and downstream, respectively (see Fig. 13d and e). Meanwhile, the 1-flame stays at almost the same location. Afterwards, the 2-flame splits into two parts (the red long arrow in Fig. 13e). The 5-flame in Fig. 13d is enlarged and merges with the left part of 2-flame, as shown in Fig. 13e. Then, the 2-flame in Fig. 13e shifts downstream further (Fig. 13f). The 4-flame in Fig. 13e which shifts downstream will merge with the 5-flame which shifts upstream in Fig. 13e, and a new 4-flame is generated in Fig. 13f. Meanwhile, the 1-flame shifts upstream very slowly (see Fig. 13). Fig. 17 presents that the moving distance of 1-flame is only  $\sim 0.25$  mm from  $t = 2.00$  ms to  $t = 2.10$  ms. This is mainly because the flow speed and gas temperature before the flame front increase slightly during this time period (see Fig. 17). The calculating result shows that the flow speed before the flame front increases from 16.31 m/s to 17.56 m/s, and its increasing ratio is 7.66% (see Fig. 17a). In addition, Fig. 17b indicates that the unburned gas temperature before the flame front increases from 1586 K to 1710 K, and its increasing ratio is 7.82%. It can be seen that the increasing ratio of unburned gas temperature is slightly larger than that of the flow speed, which might explain why the 1-flame shifts upstream even though the moving speed is very slow.

After that, the 4-flame becomes small (see Fig. 18g), and the 1-

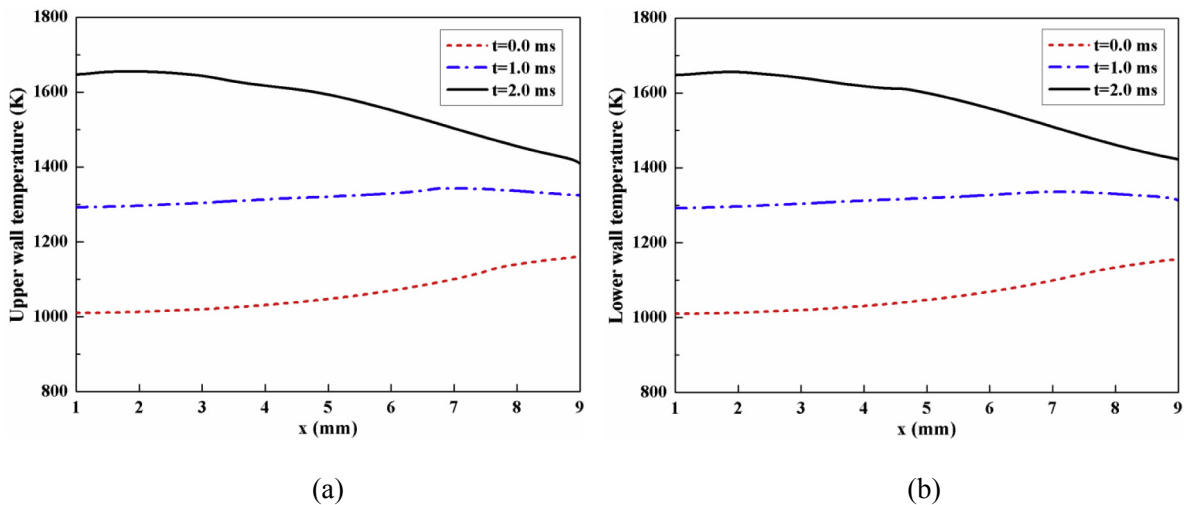


Fig. 14. Internal wall temperature of the preheating channel at  $\phi = 0.75$ : (a) upper wall surface ( $y = 1.5$  mm,  $1.0$  mm  $\leq x \leq 9.0$  mm); (b) lower wall surface ( $y = 1.0$  mm,  $1.0$  mm  $\leq x \leq 9.0$  mm).

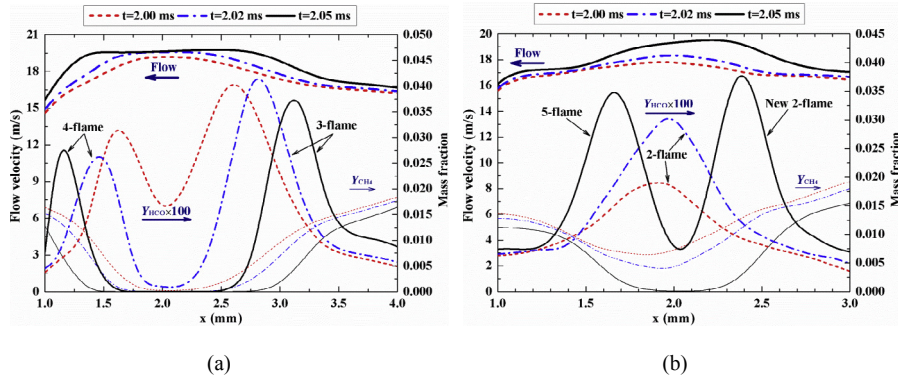


Fig. 15. Mass fractions of CH<sub>4</sub> (the finest lines) and HCO, and the flow speed (the boldest lines) near the 3-flame ( $y = 1.75$  mm,  $1.0$  mm  $\leq x \leq 4.0$  mm) (a) and 2-flame ( $y = 0.75$  mm,  $1.0$  mm  $\leq x \leq 3.0$  mm) (b) at  $\phi = 0.75$ .

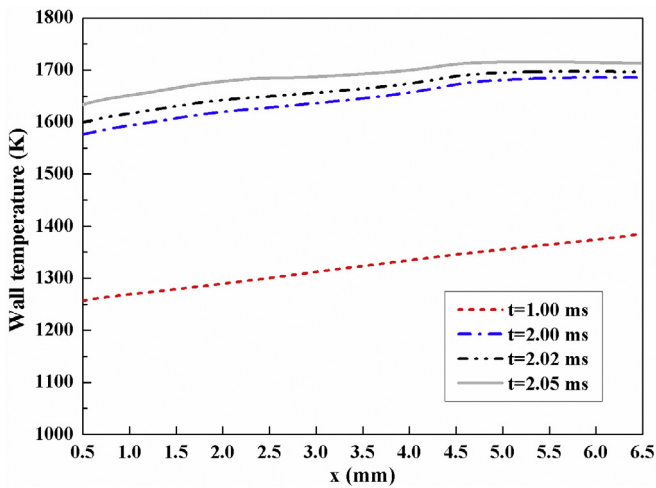


Fig. 16. Upper wall temperature of flame holder ( $y = 0.5$  mm,  $0.5$  mm  $\leq x \leq 6.5$  mm) at  $\phi = 0.75$ .

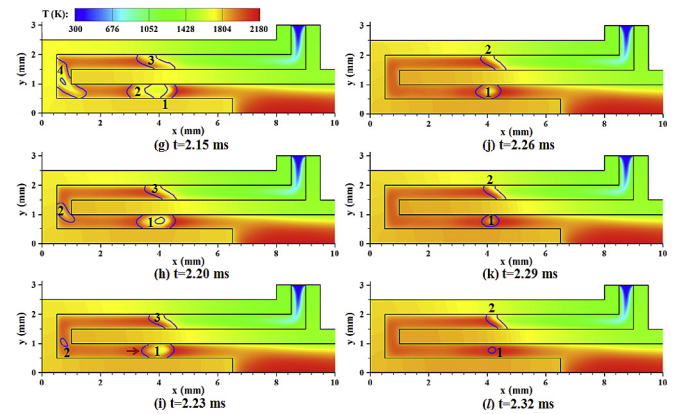


Fig. 18. Temperature contours with overlaid 15% maximum  $Y_{HCO}$  isoline (blue solid line) at  $\phi = 0.75$  (the second part of FRFP). (For interpretation of the references to colour in this figure legend, the reader is referred to the web version of this article.)

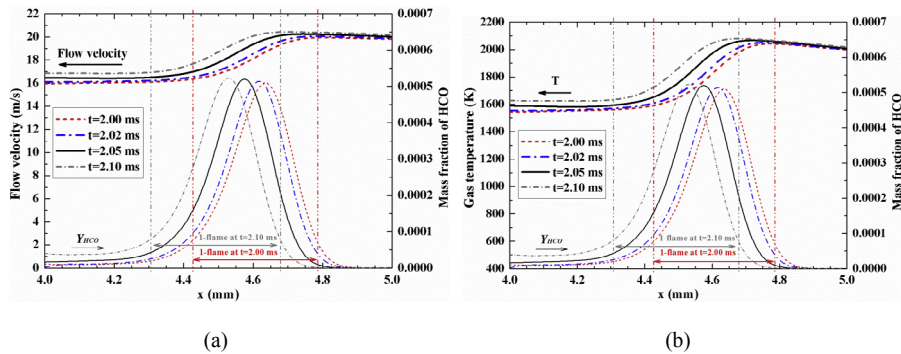


Fig. 17. Mass fraction of HCO (fine lines) with the flow speed (bold lines) (a) and gas temperature (bold lines) (b) near the 1-flame ( $y = 0.75$  mm,  $4.0$  mm  $\leq x \leq 5.0$  mm) at  $\phi = 0.75$ .

flame and 2-flame in Fig. 18g shift to each other to consume the unburned fuel between them. Then, the 4-flame in Fig. 18g becomes smaller and smaller (see 2-flame in Fig. 18h and i). Moreover, the 2-flame merges with the 1-flame in Fig. 18g, and becomes a new 1-flame in Fig. 18h and i. The left boundary of 1-flame shifts downstream (see the red arrow in Fig. 18i), and the 1-flame becomes smaller and smaller (see Fig. 18j, k and l) until extinction. Furthermore, Fig. 19 quantitatively shows the dynamic process of 1-flame at different time points. This figure indicates that the distance

between the two boundaries of 1-flame (the peak of HCO mass fraction) becomes shorter and shorter, and the fuel between the two boundaries of 1-flame is gradually consumed. At the same time, the 2-flame almost stays at the same station, and the reasons which lead to this phenomenon are the same with that of the 1-flame in Fig. 13. These mean that the methane in preheating channel behind the 2-flame in Fig. 18l is almost completely consumed, and there will exist only one flame front in the preheating channel, as shown in Fig. 20m.

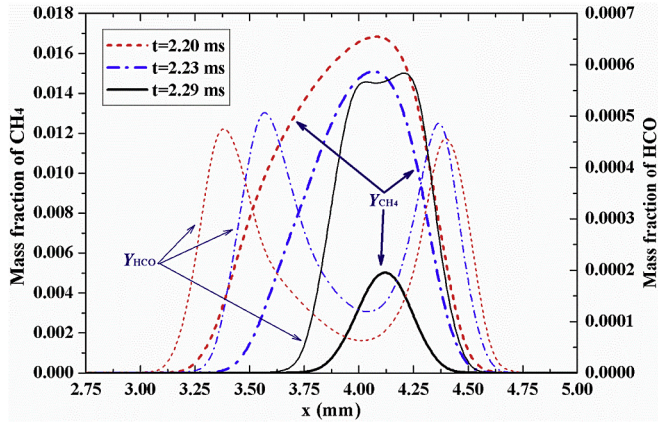


Fig. 19. Mass fraction profiles of CH<sub>4</sub> (bold lines) and HCO (fine lines) near the 1-flame ( $y = 0.75$  mm,  $2.75$  mm  $\leq x \leq 5.00$  mm) at  $\phi = 0.75$ .

Fig. 20 presents the third part of FRFP. Additionally, in order to quantitatively analyze the dynamic behavior of this flame, Fig. 21 presents the mass fraction of HCO, flow speed and gas temperature profiles near the flame front. The temperature and heat flux profiles of the external wall of preheating channel are shown in Fig. 22. Moreover, Table 3 presents the incoming unburned gas temperature and flow speed before the flame front at  $\phi = 0.75$ , which are obtained from Fig. 21. Furthermore, Fig. 23 shows the internal wall temperature and external wall temperature profiles of preheating channel. At  $t = 2.35$  ms, the only one flame front still shifts upstream (see the red arrow in Fig. 20m). This is because the incoming unburned mixture can be preheated to a high temperature (1630 K, see Table 3). Meanwhile, Fig. 22 indicates that the heat loss from the external wall of preheating channel to the environment at  $t = 2.35$  ms is also the largest, which results in the decrease of unburned mixture temperature, and this negative effect hinders the upstream movement of flame front and makes the flame front stop at a location. At  $t = 16.8$  ms, the unburned gas temperature and flow speed decrease to 1310 K and 13.39 m/s, respectively, and the flow speed takes the main role in the movement of flame front. Therefore, the flame front shifts downstream (see the red arrow in Fig. 20n). However, it is interesting to find that the incoming unburned mixture temperature increases from the 1310 K at  $t = 16.8$  ms to 1520 K at  $t = 27.3$  ms. Afterwards, the gas temperature decreases with time (see Fig. 20p and q). The reasons for this

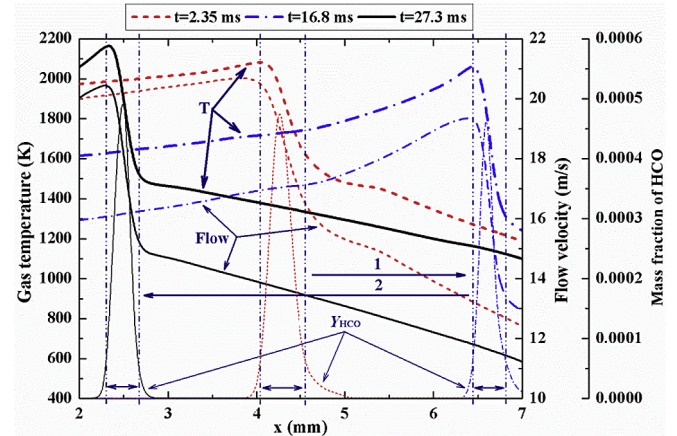


Fig. 21. Mass fraction of HCO (the finest lines), flow speed and gas temperature (the boldest lines) near the flame front ( $y = 1.75$  mm,  $2.0$  mm  $\leq x \leq 7.0$  mm) at  $\phi = 0.75$ .

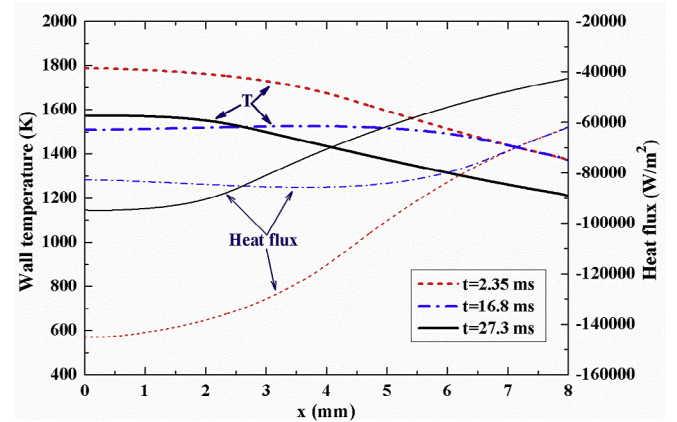


Fig. 22. The temperature (bold lines) and heat flux (fine lines) profiles of the external wall of preheating channel ( $y = 2.5$  mm,  $0.0$  mm  $\leq x \leq 8.0$  mm) at  $\phi = 0.75$  (the negative value of heat flux means heat loss to the environment).

Table 3

Incoming unburned mean gas temperature and flow speed before the flame front at  $\phi = 0.75$  for different time points.

Time (ms)	Gas temperature (K)	Flow speed (m/s)
2.35	1630	16.55
16.8	1310	13.39
27.3	1520	15.21

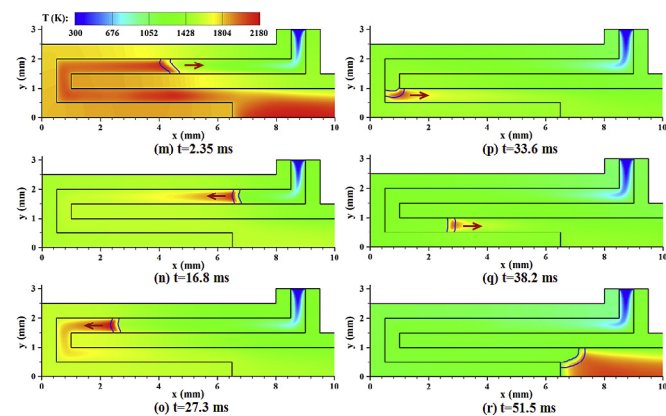
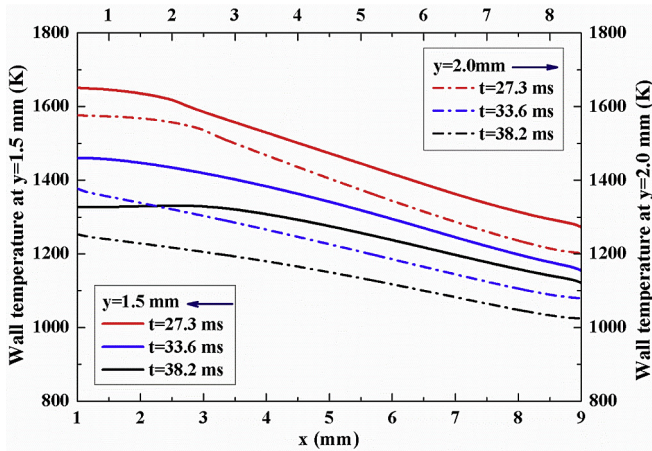


Fig. 20. Temperature contours with overlaid 15% maximum  $Y_{HCO}$  isoline (blue solid line) at  $\phi = 0.75$  (the third part of FRFP). (For interpretation of the references to colour in this figure legend, the reader is referred to the web version of this article.)

seemingly abnormal phenomenon can be got from Figs. 21 and 22. At  $t = 27.3$  ms, the distance of preheating unburned fuel mixture in preheating channel is longer even though the wall temperature of preheating channel decreases to some extent, but the lower wall temperature of preheating channel makes the heat loss smaller at the same time (see Fig. 22). As a result, the longer preheating distance and smaller heat loss lead to a higher unburned mixture temperature before the flame front at  $t = 27.3$  ms. Afterwards, when the flame front is within the preheating channel between the internal wall of preheating channel and flame holder, the external wall of preheating channel ( $y = 2.0$  mm) cannot be directly heated by the flame, and the area of high temperature exhaust mixture behind the flame front in the preheating channel decreases with time. As a result, the wall temperature level of preheating channel decreases further (see Fig. 23), and this negative effect makes the



**Fig. 23.** The internal wall temperature ( $y = 1.5$  mm,  $1.0$  mm  $\leq x \leq 9.0$  mm) and the external wall temperature ( $y = 2.0$  mm,  $0.5$  mm  $\leq x \leq 8.5$  mm) profiles of preheating channel at  $\phi = 0.75$ .

gas temperature decrease with time, which leads to a smaller burning velocity. Meantime, there is no methane in the downstream preheating channel after the flame front. Therefore, the flame front shifts to the outlet of preheating channel step by step (see Fig. 20o, p and q) and is blown out of the preheating channel (see Fig. 20r). Finally, a pulsating flame behavior occurs in the combustion chamber (see Figs. 20r, 13a and b), which is similar with the case of  $\phi = 0.725$ .

In addition, it is interesting to observe that the shape of flame front at  $t = 2.35$  ms is more oblique than that at  $t = 16.8$  ms in Fig. 20. The reasons for this phenomenon can be got from Fig. 24. At  $t = 2.35$  ms, as the gas temperature between the internal wall of preheating channel ( $y = 1.0$  mm) and flame holder ( $y = 0.5$  mm) is high (see Fig. 20m), the internal wall temperature of preheating channel near the flame front is obviously higher than the external wall temperature of preheating channel (see Fig. 24a). From Fig. 24a the internal wall temperature of preheating channel ( $y = 1.5$  mm) at the maximum of  $Y_{HCO}$  is  $\sim 1790$  K (see the horizontal blue dashed line), and the external wall temperature of preheating channel ( $y = 2.0$  mm) at the maximum of  $Y_{HCO}$  is  $\sim 1670$  K (see the horizontal black dashed line), *i.e.*, the temperature difference between them is 120 K. As the higher wall temperature results in a faster burning velocity, which makes the lower boundary of flame front near the internal wall of preheating channel shift upstream. As a result, the horizontal distance between the upper and lower boundaries of

flame front at  $t = 2.35$  ms is  $\sim 0.35$  mm (see the distance between the two vertical dashed lines). However, after  $t = 2.35$  ms, there is no unburned fuel in preheating channel, so the high-temperature exhaust mixture in the preheating channel and combustion chamber will be cooled due to the heat loss from the external wall of preheating channel and the combustion chamber wall, which will reduce the wall temperature of preheating channel (see Fig. 24b). Fig. 24b shows that the wall temperature of preheating channel decreases significantly, and the results indicate that the internal wall temperature of preheating channel at the maximum of  $Y_{HCO}$  is  $\sim 1510$  K (see the horizontal blue dashed line), and the external wall temperature of preheating channel at the maximum of  $Y_{HCO}$  is  $\sim 1470$  K (see the horizontal black dashed line), *i.e.*, the temperature difference between the upper and lower boundaries of flame front is very small ( $\sim 0.03$  mm, see the distance between the two vertical dashed lines). In one word, a higher wall temperature can make the flame front near this wall shift upstream. From the above results, we can see that the process that the flame flashes back to the preheating channel from the combustion chamber (from  $t = 1.00$  ms–2.35 ms) is more complex than the process that the flame blows out of the preheating channel (from  $t = 16.8$  ms–51.5 ms).

Fig. 25 shows the frequencies of FRFP at different equivalence

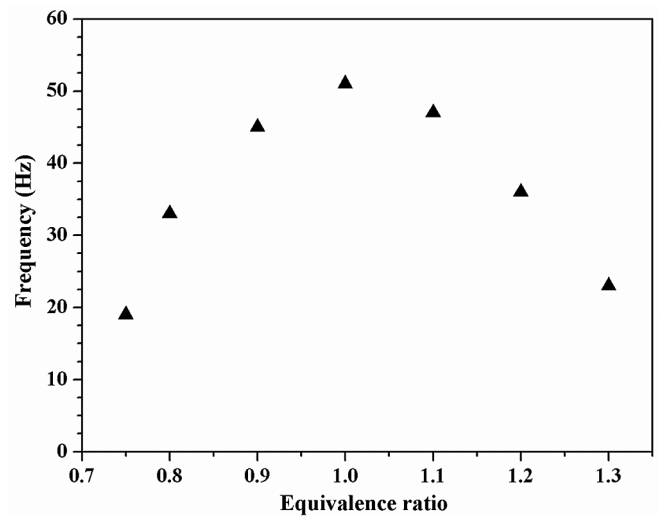


**Fig. 25.** Frequencies of FRFP at different equivalence ratios.

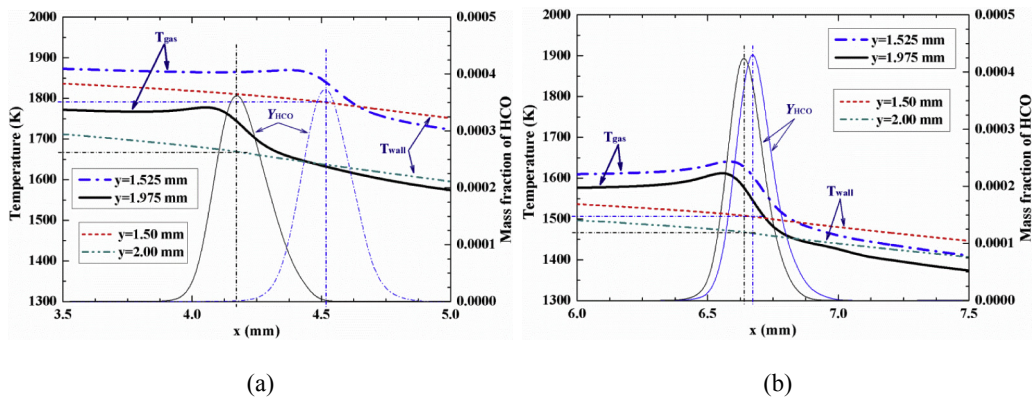


**Fig. 24.** The gas temperature (the boldest lines) and mass fraction of HCO (the finest lines) near the inner wall of preheating channel ( $y = 1.525$  mm and 1.975 mm) and the wall temperature at  $y = 1.50$  mm and 2.00 mm near the flame front at  $t = 2.35$  ms (a) and 16.8 ms (b).

ratios. The frequency increases firstly and then decreases with the increase of equivalence ratio. This is mainly because that the competitive effect between the flow speed and burning velocity is more remarkable when the equivalence ratio is closer to the stoichiometric ratio.

#### 4. Conclusions

A micro combustor with a plate flame holder and preheating channels was developed in our previous work, and this combustor can be used as heat resource for the micro- or meso-scale TPV (Thermophotovoltaic) and propulsion system. The present paper investigates the flammable range based on equivalence ratio, and some dynamic flame behaviors are also observed, which include the flame blow-off, pulsating flame and the flame with repetitive flashback and pulsating (FRFP). For the lean fuel, a higher equivalence ratio of incoming unburned mixture leads to a faster burning velocity and a higher preheating temperature. Although a higher preheating temperature can further increase the burning velocity, the incoming flow speed is also enlarged due to the remarkable thermal expansion effect. As known, the faster burning velocity pulls the flame upstream, but the bigger flow speed pushes the flame downstream. Our analysis indicates that the flame behaviors are mainly determined by the competitive effect of the burning velocity and incoming flow speed. When the equivalence ratio is too small (such as the case at  $\phi = 0.5$ ), the smaller burning velocity under the lower preheating temperature and equivalence ratio than the incoming flow speed makes the flame blow out of the combustion chamber. When the equivalence ratio increases from 0.5 to 0.525, the burning velocity reaches a static balance with the flow speed, thus the flame can remain stable. However, when the equivalence ratio increases further (such as at  $\phi = 0.725$ ), the burning velocity reaches a dynamic balance with the flow speed in the combustion chamber, which results in a pulsating behavior. Nevertheless, the burning velocity at  $\phi = 0.75$  is enough fast to make the flame flash back to the preheating channel. In this stage, the burning velocity can only reach a dynamic balance with the flow speed in the combustion chamber and preheating channel, which leads to the formation of the flame with repetitive flashback and pulsating. In addition, the competition between the burning velocity and flow speed can also explain the dynamic flame behaviors under the rich fuel condition, which also presents four kinds of flame behavior.

#### Acknowledgements

This work was supported by the Natural Science Foundation of China (Nos. 51522603, 51390494) and the China Postdoctoral Science Foundation (2016M600591).

#### References

- [1] Fernandez-Pello AC. Micro power generation using combustion: issues and approaches. *Proc Combust Inst* 2002;29:883–99.
- [2] Maruta K. Micro and mesoscale combustion. *Proc Combust Inst* 2011;33(1):125–50.
- [3] Ju Y, Maruta K. Microscale combustion: technology development and fundamental research. *Prog Energ Combust Sci* 2011;37(6):669–715.
- [4] Maruta K, Kataoka T, Kim NI, Minaev S, Fursenko R. Characteristics of combustion in a narrow channel with a temperature gradient. *Proc Combust Inst* 2005;30(2):2429–36.
- [5] Fan AW, Wan JL, Maruta K, Nakamura H, Yao H, Liu W. Flame dynamics in a heated meso-scale radial channel. *Proc Combust Inst* 2013;34(2):3351–9.
- [6] Kumar S, Maruta K, Minaev S. On the formation of multiple rotating Pelton-like flame structures in radial microchannels with lean methane–air mixtures. *Proc Combust Inst* 2007;31(2):3261–8.
- [7] Alipoor A, Mazaheri K. Studying the repetitive extinction-ignition dynamics for lean premixed hydrogen–air combustion in a heated microchannel. *Energy* 2014;73:367–79.
- [8] Alipoor A, Mazaheri K. Combustion characteristics and flame bifurcation in repetitive extinction-ignition dynamics for premixed hydrogen–air combustion in a heated micro channel. *Energy* 2016;109:650–63.
- [9] Rana U, Chakraborty S, Som SK. Thermodynamics of premixed combustion in a heat recirculating micro combustor. *Energy* 2014;68:510–8.
- [10] Chen W-H, Lin S-C. Reaction phenomena of catalytic partial oxidation of methane under the impact of carbon dioxide addition and heat recirculation. *Energy* 2015;82:206–17.
- [11] Zarvandi J, Tabejamaat S, Baigmohammadi M. Numerical study of the effects of heat transfer methods on CH<sub>4</sub>/(CH<sub>4</sub> + H<sub>2</sub>)-AIR pre-mixed flames in a micro-stepped tube. *Energy* 2012;44(1):396–409.
- [12] Epstein AH, Senturia SD, Anathasuresh G, Ayon A, Breuer K, Chen KS, et al. Power MEMS and microengines. In: *Transducers '97, 1997 international conference on solid-state sensors and actuators*, vol. 2; 1997. p. 753–6.
- [13] Spadaccini CM, Peck J, Waitz IA. Catalytic combustion systems for microscale gas turbine engines. *J Eng Gas Turbines Power* 2007;129(1):49–60.
- [14] Spadaccini CM, Mehra A, Lee J, Zhang X, Lukachko S, Waitz IA. High power density silicon combustion systems for micro gas turbine engines. *J Eng Gas Turbines Power* 2003;125(3):709–19.
- [15] Kim N, Kato S, Kataoka T, Yokomori T, Maruyama S, Fujimori T, et al. Flame stabilization and emission of small Swiss-roll combustors as heaters. *Combust Flame* 2005;141(3):229–40.
- [16] Kuo CH, Ronney PD. Numerical modeling of non-adiabatic heat-recirculating combustors. *Proc Combust Inst* 2007;31(2):3277–84.
- [17] Gauthier GP, Watson GMG, Bergthorson JM. Burning rates and temperatures of flames in excess-enthalpy burners: a numerical study of flame propagation in small heat-recirculating tubes. *Combust Flame* 2014;161(9):2348–60.
- [18] Jiang LQ, Zhao DQ, Guo CM, Wang XH. Experimental study of a plate-flame micro combustor burning DME for thermoelectric power generation. *Energy Convers Manag* 2011;52(1):596–602.
- [19] Wang H, Wei C, Zhao P, Ye T. Experimental study on temperature variation in a porous inert media burner for premixed methane air combustion. *Energy* 2014;72:195–200.
- [20] Baigmohammadi M, Sarrafan Sadeghi S, Tabejamaat S, Zarvandi J. Numerical study of the effects of wire insertion on CH<sub>4</sub>(methane)/AIR pre-mixed flame in a micro combustor. *Energy* 2013;54:271–84.
- [21] Veeragavan A. On flame propagation in narrow channels with enhanced wall thermal conduction. *Energy* 2015;93:631–40.
- [22] Yang WM, Chou SK, Shu C, Li Xue H. Experimental study of micro-thermophotovoltaic systems with different combustor configurations. *Energy Convers Manag* 2007;48(4):1238–44.
- [23] Khandelwal B, Deshpande AA, Kumar S. Experimental studies on flame stabilization in a three step rearward facing configuration based micro channel combustor. *Appl Therm Eng* 2013;58(1–2):363–8.
- [24] Wan JL, Fan AW, Yao H, Liu W. Experimental investigation and numerical analysis on the blow-off limits of premixed CH<sub>4</sub>/air flames in a mesoscale bluff-body combustor. *Energy* 2016;113:193–203.
- [25] Wan JL, Fan AW, Liu Y, Yao H, Liu W, Gou XL, et al. Experimental investigation and numerical analysis on flame stabilization of CH<sub>4</sub>/air mixture in a meso-scale channel with wall cavities. *Combust Flame* 2015;162(4):1035–45.
- [26] Wan JL, Fan AW, Yao H, Liu W. Effect of thermal conductivity of solid wall on combustion efficiency of a micro-combustor with cavities. *Energy Convers Manag* 2015;96:605–12.
- [27] Di Stazio A, Chauveau C, Dayma G, Dagaut P. Oscillating flames in micro-combustion. *Combust Flame* 2016;167:392–4.
- [28] Akram M, Kumar S. Experimental studies on dynamics of methane–air premixed flame in meso-scale diverging channels. *Combust Flame* 2011;158(5):915–24.
- [29] Pizza G, Frouzakis CE, Mantzaras J, Tomboulides AG, Boulouchos K. Dynamics of premixed hydrogen/air flames in microchannels. *Combust Flame* 2008;152(3):433–50.
- [30] Brambilla A, Frouzakis CE, Mantzaras J, Bombach R, Boulouchos K. Flame dynamics in lean premixed/air combustion in a mesoscale channel. *Combust Flame* 2014;161(5):1268–81.
- [31] Baigmohammadi M, Tabejamaat S, Faghani-Lamraski M. Experimental study on the effects of mixture flow rate, equivalence ratio, oxygen enhancement, and geometrical parameters on propane–air premixed flame dynamics in non-adiabatic meso-scale reactors. *Energy* 2017;121:657–75.
- [32] Lee BJ, Yoo CS, Im HG. Dynamics of bluff-body-stabilized premixed hydrogen/air flames in a narrow channel. *Combust Flame* 2015;162(6):2602–9.
- [33] Lee BJ, Im HG. Dynamics of bluff-body-stabilized lean premixed syngas flames in a meso-scale channel. *Proc Combust Inst* 2017;36(1):1569–76.
- [34] Wan JL, Fan AW. Effect of solid material on the blow-off limit of CH<sub>4</sub>/air flames in a micro combustor with a plate flame holder and preheating channels. *Energy Convers Manag* 2015;101:552–60.
- [35] Wan JL, Fan AW, Yao H. Effect of the length of a plate flame holder on flame blowout limit in a micro-combustor with preheating channels. *Combust Flame* 2016;170:53–62.
- [36] Khandelwal B, Sahota GPS, Kumar S. Investigations into the flame stability limits in a backward step micro scale combustor with premixed methane–air mixtures. *J Micromech Microeng* 2010;20(9):095030.
- [37] Kim NI, Aizumi S, Yokomori T, Kato S, Fujimori T, Maruta K. Development and scale effects of small Swiss-roll combustors. *Proc Combust Inst* 2007;31(2):3243–50.
- [38] Ma Q, Fang R, Xiang L. *Handbook of thermo-physical properties*. Beijing: China

- Agricultural Machinery Press; 1986 (in chinese).
- [39] Kee RJ, Grcar JF, Smooke MD, Miller JA. Sandia national laboratories report, SAND85–8240. 1994.
- [40] Kee RJ, Rupley FM, Miller JA. Sandia national laboratories report, SAND87–8215B. 1990.
- [41] Kee RJ, Grcar JF, Smooke MD, Miller JA. Sandia national laboratories report, SAND85–8240. 1985.
- [42] Fluent 6.3. User's guide. Lebanon, New Hampshire: Fluent Inc; 2006.
- [44] Chen Z. On the accuracy of laminar flame speeds measured from outwardly propagating spherical flames: methane/air at normal temperature and pressure. *Combust Flame* 2015;162(6):2442–53.
- [45] Law CK. *Combustion physics*. Cambridge: Cambridge University press; 2006.
- [46] Nikolaou ZM, Swaminathan N. Heat release rate markers for premixed combustion. *Combust Flame* 2014;161(12):3073–84.